Optimization of the volume reconstruction for classical Tomo-PIV algorithms (MART, BIMART and SMART): synthetic and experimental studies

Lionel Thomas, Benoit Tremblais, Laurent David

Optimization of the volume reconstruction for classical Tomo-PIV algorithms (MART, BIMART and SMART): synthetic and experimental studies

L Thomas[1], **B Tremblais**[2] **and L David**[1]

[1] Institut P', UPR3346, CNRS–Université de Poitiers–ENSMA, Téléport 2, 11 Boulevard Marie et Pierre Curie BP 30179, F-86962 Futuroscope Chasseneuil Cedex, France
[2] Université de Poitiers, Laboratoire XLIM, Département SIC, CNRS 7252, Téléport 2, avenue Clément ADER BP 40109, 86961 Futuroscope Chasseneuil, France

E-mail: lionel.thomas@univ-poitiers.fr

Abstract

Optimization of multiplicative algebraic reconstruction technique (MART), simultaneous MART and block iterative MART reconstruction techniques was carried out on synthetic and experimental data. Different criteria were defined to improve the preprocessing of the initial images. Knowledge of how each reconstruction parameter influences the quality of particle volume reconstruction and computing time is the key in Tomo-PIV. These criteria were applied to a real case, a jet in cross flow, and were validated.

Keywords: Tomo-PIV, optimization, MART, SMART, BIMART

1. Introduction

Tomographic reconstruction techniques appeared in 1970 (Gordon *et al* 1970). These techniques were first used in the medical field, and in this context internal organs can be reconstructed in a computational domain and analyzed. This type of tomography relies on essentially infinite viewing or sampling angles on a stationary target. With the introduction of Tomo-PIV, tomographic algebraic reconstruction techniques (ART) have been extended to the PIV field to reconstruct 3D particle distribution to study complex flows. These methods are well suited to resolve the problem of an indeterminate system, but are very expensive in computation time and memory storage. The multiplicative ART (MART) method is the algebraic technique mostly used in Tomo-PIV. This method has proved its relevance for reconstructing objects with large velocity gradient (Verhoeven 1993). It has also been shown that MART gives a better result than ART with more distinct particles. Tomographic reconstruction results realized with MART have shown that the particles positions are reconstructed correctly (Elsinga 2008).

Different comparisons between algebraic reconstruction techniques such as ART, adaptive ART, SIRT (simultaneous iterative reconstruction technique), simultaneous ART, MART and simultaneous MART (SMART) have already been performed and results showed that MART and SMART were the more robust reconstruction techniques (Atkinson and Soria 2007, 2009).

A drawback of such reconstruction techniques is the computational cost. Discetti and Astarita (2011a) proposed a multi-resolution strategy to reduce it. Bilsky *et al* (2012) introduced the MENT algorithm for Tomo-PIV which is even faster than SMART but seems to be slightly less accurate than the previous algorithms. Most of the ways to accelerate the computation are based now on the massive parallelization on CPUs or GPUs. Recently, more efforts have been dedicated to accelerate the correlation algorithms.

Recently, the optimization of the technique has slowed somewhat and a survey of the literature suggests

that, increasingly, published material is dedicated to the applications of the technique. The recent review by Scarano (2013) shows the diversity of the applications using Tomo-PIV.

In this paper, we wanted to show that the classical reconstruction algorithms (MART and SMART) have not yet been optimized and that some parameters can be tuned to increase the reconstruction quality and to reduce the reconstruction time. In section 2, the volume reconstruction problem is detailed and the methodology is described. In section 3, the influence on synthetic images of all the parameters is studied and an optimization is proposed. An optimized algorithm is applied on experimental images in section 4 and some specific problems are addressed.

2. Volume reconstruction

2.1. Definitions

In this part, the problem of volume reconstruction is considered as an inversion of the projection operator. Let $\mathcal{V}$ be a volume of particles illuminated by a laser sheet. N cameras focus on this volume, generating N images $\mathcal{I}_n$ with $1 \leqslant n \leqslant N$. The light intensity at a point $\boldsymbol{X}$ in $\mathcal{V}$ is $E(\boldsymbol{X})$. The intensity of the light at a point $\boldsymbol{x}$ in the image $\mathcal{I}_n$ is $I_n(\boldsymbol{x})$. The geometric correspondence between a point $\boldsymbol{X}$ in the volume and a point $\boldsymbol{x}$ in the image $\mathcal{I}_n$ is determined by the camera optical arrangement. It is described by a projection function ψ_n defined in equation (1):

$$\psi_n(\boldsymbol{X}) = \boldsymbol{x}. \tag{1}$$

It is considered that the projection of a point in the volume on a given image is unique. A back-projection function can also be defined; however, for a given point $\boldsymbol{x}$ in the image $\mathcal{I}_n$, there is not one unique corresponding point in the volume but a set of points. This set of points, in the volume whose projection is $\boldsymbol{x}$, is a curve called the line-of-sight $(\mathrm{LOS})_n(\boldsymbol{x})$. In the remainder of this paper, $\boldsymbol{e}_Z$ is the direction perpendicular to the laser sheet. All the lines of sight can be parametrized using the variable Z. For a given Z, the back-projection function can be defined such as given in equation (2):

$$\psi_n^{-1}(\boldsymbol{x},\, Z) = (X,\, Y,\, Z). \tag{2}$$

In practice, these projection and back-projection functions are obtained through a rigorous calibration procedure.

To obtain a relation between E and I_n, the light propagation must be taken into account and some assumptions made on the medium constituted by the particles. If the particles are small enough to diffuse the light, then the medium can be considered transparent and the particles are modeled as localized light sources. In PIV applications, the concentration of particles is sufficiently sparse that the light attenuation can be considered negligible. The optical system must also be considered as some defaults can be accounted for. An optical transfer function (OTF) (Schanz *et al* 2010) can be introduced. The projection of a Dirac light distribution in the volume is therefore a distribution of light in the image. The relation between E and I_n is given in equation (3):

$$I_n(\boldsymbol{x}) = \int_{\boldsymbol{x}+\boldsymbol{u}\in\mathcal{I}_n} \phi(\boldsymbol{x};\boldsymbol{u}) \int_{Z_{\min}}^{Z_{\max}} E(\psi_n^{-1}(\boldsymbol{x}+\boldsymbol{u},\, Z)) \times \left|\left| \frac{\partial \psi_n^{-1}}{\partial Z} \right|\right| \mathrm{d}Z\, \mathrm{d}\boldsymbol{u}, \tag{3}$$

where ϕ is the OTF. In this paper, a Dirac function in the volume gives a Dirac function in the images. Hence, equation (3) simplifies to equation (4):

$$I_n(\boldsymbol{x}) = \int_{Z_{\min}}^{Z_{\max}} E(\psi_n^{-1}(\boldsymbol{x},\, Z)) \left|\left| \frac{\partial \psi_n^{-1}}{\partial Z} \right|\right| \mathrm{d}Z. \tag{4}$$

Equation (4) describes the direct problem of the projection. The volume reconstruction in Tomo-PIV consists in the inversion of this equation. It is an ill-posed inverse problem. The solution is not unique and has been shown to be very sensitive to noise. This problem can be solved numerically using an inversion in Fourier space, but in the case of a restricted number of views, iterative methods are more appropriate (Herman 1980). These iterative methods are based on a discretization of the problem and are described in the next section.

2.2. Discretization

Let the dimensions of the camera images be $n_i \times n_j$ where i and j refer to the row and column dimension respectively. The position of a pixel is given by $\boldsymbol{x}_p = (i,\ j)$. It is possible to use a 1D representation using the index $p = i + n_i j$. The intensity distribution on each image $\mathcal{I}_n$ is decomposed on a finite set of pixels following equation (5):

$$I_n(\boldsymbol{x}) = \sum_{p=0}^{P_n} I_{np} \mathrm{pix}(\boldsymbol{x} - \boldsymbol{x}_p). \tag{5}$$

The function pix() describes the pixel basis function. In this paper, a squared function of side length equal to 1 is considered, defined in equation (6):

$$\mathrm{pix}(\boldsymbol{x}) = \chi(x)\chi(y), \tag{6}$$

where χ is the characteristic function over the interval $[-0.5,\, 0.5]$. The intensity of one pixel is then given in equation (7):

$$I_{np} = \int_{\mathcal{I}_n} \mathrm{pix}(\boldsymbol{x} - \boldsymbol{x}_p) \int_{Z_{\min}}^{Z_{\max}} E(\psi_n^{-1}(\boldsymbol{x},\, Z)) \left|\left| \frac{\partial \psi_n^{-1}}{\partial Z} \right|\right| \mathrm{d}Z\, \mathrm{d}\boldsymbol{x}. \tag{7}$$

The volume can be discretized in the same way. The dimension of the volume is $N_K \times N_I \times N_J$. The origin of the volume is $(X_0,\, Y_0,\, Z_0)$. The voxel real dimensions are ΔX, ΔY and ΔZ. The position of a voxel is given by $\boldsymbol{X}_V = (X_0 + J\Delta X,\, Y_0 + I\Delta Y,\, Z_0 + K\Delta Z)$. The index used for a 1D representation is given by $V = I + N_I J + N_I N_J K$.

The voxel basis function is defined in equation (8) as a squared function but other functions could be considered (Petra *et al* 2009):

$$\mathrm{vox}(\boldsymbol{X}) = \chi\left(\frac{X}{\Delta X}\right)\chi\left(\frac{Y}{\Delta Y}\right)\chi\left(\frac{Z}{\Delta Z}\right). \tag{8}$$

The intensity of one pixel is then given in equation (9):

$$I_{np} = \sum_V w_{pV} E_V, \tag{9}$$

where w_{pV} defined in equation (10) is the geometric interaction between the pixel np and the voxel V:

$$w_{pV} = \int_{\mathcal{I}_n} \mathrm{pix}(\boldsymbol{x} - \boldsymbol{x}_p) \int_{Z_V - \frac{\Delta Z}{2}}^{Z_V + \frac{\Delta Z}{2}} \chi\left(\frac{X - X_V}{\Delta X}\right) \chi\left(\frac{Y - Y_V}{\Delta Y}\right) \times \left|\left| \frac{\partial \psi_n^{-1}}{\partial Z} \right|\right| \mathrm{d}Z\, \mathrm{d}\boldsymbol{x}, \quad (10)$$

where $X = \psi_n^{-1}(\boldsymbol{x}, Z).\boldsymbol{e}_X$ and $Y = \psi_n^{-1}(\boldsymbol{x}, Z).\boldsymbol{e}_Y$. w_{pV} is the volume of the intersection between the voxel (a cube in our case) and a pyramid, which cannot be calculated exactly. Different approximations are proposed in the literature. Several methods are tested in this paper.

- *Direct.* The simplest model considers that if the center of the voxel V is projected inside the pixel p, $w_{pV} = 1$, otherwise, $w_{pV} = 0$.
- *Bilinear.* w_{pV} is given here by the weight the voxel V would have if we wanted to interpolate, with a bilinear method, the volume intensity at the position of the back projection of pixel p.
- *LOS length.* The voxel V is modeled by a sphere and the pixel by a point. w_{pV} is the length of the intersection between the sphere and the LOS divided by the sphere diameter.
- *Gaussian.* w_{pV} is a Gaussian function depending on the distance r between the projection of the voxel center and the pixel considered. $w_{pV} = \exp(-r^2 \log 20)$.
- *Disc-intersect.* As introduced by Lamarche and Leroy (1990), the pixel is approximated by a disc of radius $R = 1/\sqrt{2}$ and the voxel by a sphere of the same radius. The pyramid is approximated by a cylinder of radius R. w_{pV} is the volume of the intersection of the cylinder and the sphere divided by the sphere volume. r is defined as the distance between the center of pixel p and the projection of the voxel V, if $d \geqslant 2r$, $w_{pV} = 0$, otherwise $w_{pV} = \frac{2}{\pi}(2R^2 \mathrm{acos}(r/2R) - r/2\sqrt{4R^2 - r^2})$
- *Subvoxel.* The voxel V is decomposed into $nsx \times nsy \times nsz$ subvoxels. w_{pV} is the proportion of subvoxels that are projected inside the pixel p.

Some of these models are plotted in the figure 1. Except for the subpixels and subvoxels approximations, all the models depend only on the distance between the projection of the voxel center and the pixel center (Thomas *et al* 2010). It is supposed that they are uniform for all voxels and pixels. This hypothesis can be reduced using the OTF functions. For example, the Gaussian function with circular shape can be replaced by a Gaussian function with an elliptical shape and variable radius to take into account the variation of the voxels' projection size and some optical aberrations such as defocusing, blurring or astigmatism. The main drawback of using OTF functions is that a calibration is needed to adjust these parameters (Schanz *et al* 2010).

The discretization of the problem leads to the linear problem given in equation (9) to invert. Many algorithms have been developed so far. The most commonly used in Tomo-PIV are presented in section 2.3.

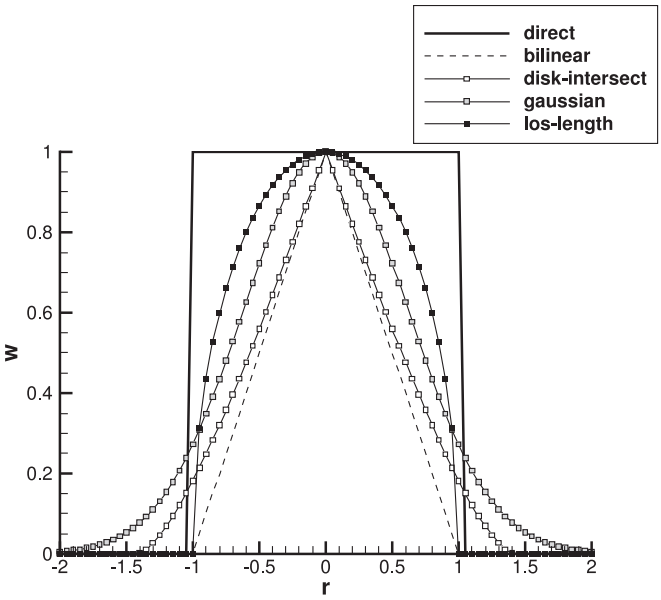

Figure 1. 1D representation of some of the projection models.

2.3. Reconstruction algorithms

As the problem is ill posed, all the methods aim to minimize the difference between the images' intensity and the projected volume intensity. Two strategies are mainly used to achieve this minimization: using a sparse norm (Petra *et al* 2007) or maximizing the entropy. In this paper, the last family of algorithms, MART, SMART and BIMART, which maximize the entropy, are discussed.

- *Multiplicative algebraic reconstruction technique.* It is the first algorithm used in Tomo-PIV. It was introduced in the domain by Elsinga *et al* (2006). It is based on global entropy maximization. For each pixel p, the intensity of all the voxels along $\mathrm{LOS}(p) = \{V \in \mathcal{V},\ w_{pV} > 0\}$ is updated iteratively following equation (11):

$$E_V^{k+1} = E_V^k \left(\frac{I_p}{\sum_V w_{pV} E_V^k}\right)^{\mu w_{pV}}. \quad (11)$$

  MART converges toward a positive solution. μ is a relaxation parameter.
- *Simultaneous multiplicative algebraic reconstruction technique).* It was used in Tomo-PIV for the first time by Atkinson and Soria (2009). It is based on a maximization of global cross-entropy. The intensity of all the voxels is updated iteratively following equation (12):

$$E_V^{k+1} = E_V^k \left(\Pi_p \left(\frac{I_p}{\sum_V w_{pV} E_V^k}\right)^{\mu w_{pV}}\right)^{1/N}. \quad (12)$$

  SMART converges toward a positive solution. The main advantage of SMART is that it can use less memory than MART, using a proper initialization (see section 2.4).
- *Block iterative MART.* This method has been introduced by Byrne (2009). It is a generalization of both MART

and SMART. It is based on the maximization of the cross-entropy. Each image is divided in Q blocks $\mathcal{B}_q$, $1 \leqslant q \leqslant Q$. The algorithm is given in equation (13):

$$E_V^{k+1} = E_V^k \Pi_{p\in\mathcal{B}_q} \left(\frac{I_p}{\sum_V w_{pV} E_V^k} \right)^{\gamma_q \delta_V w_{pV}}. \qquad (13)$$

There is a condition on γ_q and δ_V: $0 < s_{qV}\gamma_q\delta V \leqslant 1$. s_{qV} is defined as $\sum_{p\in\mathcal{B}_q} w_{pV}$. Similarly, s_V is given by $\sum_{q=1}^{Q} s_{qV}$. There are two ways two define δ_V and γ_q:

* $\delta_V = 1$ and $\gamma_q = (\max_V\{s_{qV}\})^{-1}$
* $\delta_V = s_V^{-1}$ and $\gamma_q = (\max_V\{s_{qV}s_V^{-1}\})^{-1}$.

In practice, we considered $\gamma_q\delta_V = \mu$ in order to reduce the computation time slightly.

2.4. Initialization

All these algorithms need to be initialized. The simplest way to initialize the volume is to set all the voxels' intensities to 1. This initialization is generally not ideal because it is far from the final solution, a volume of predominantly zero intensity voxels. One way to improve this is to initialize the volume with a first guess. Several procedures have been implemented so far. Worth and Nickels (2008) suggested to use a minimum LOS initialization (minLOS): each voxel is initialized with the minimum value of each pixel in direct interaction with it. As in ideal images, the background has a zero value, this first guess of the volume is sparse. The main interest is that, in further reconstruction iterations, there is no longer any need to process zero value (or black) voxels. Although this is a non-iterative and therefore fast method to determine particle locations in the volume, it is not sufficient to obtain a proper solution by itself because it does not reduce the ghost particles' intensity. Another similar way to initialize the volume is the multiplicative LOS (MLOS): instead of taking the minimum value, the geometric average is considered.

Another technique to speed up the process is to use a fast reconstruction algorithm first and then switch to a slower but more precise algorithm. In this paper, a fast version of the SMART algorithm, called the SMART_FAST, was used. It is similar to SMART but with a fast implementation of the bilinear weighting function. For each voxel, the weight is computed using only 4 pixels per camera. The initial solutions are compared and also the solution after 5 MART iterations and 15 SMART iterations. The *smart n* initialization corresponds to n iterations of SMART_FAST.

3. Synthetic data results

To characterize the different algorithms, we tested them on the same computer configuration: a single Intel Core2 T9600 2.8 GHz CPU using 4 Go RAM. All the programs were developed in C++ using the SLIP library (Tremblais *et al* 2010).

3.1. Image generator

Synthetic images were generated in this study to investigate the accuracy of the reconstructed volumes. Volumes were filled with Gaussian particles, with 3.5 voxels diameter leading to particle images of around 6 pixels in diameter. The reference concentration was chosen so the number of particles per pixel (ppp) is equal to 0.05. This ppp was computed exactly as the number of particles in the volume, divided per number of active pixels in the considered image, which are defined as the pixels whose LOS is crossing the volume. Another characteristic of the concentration of particles in the images is the image signal ratio Ns (Scarano 2013), defined as the percentage of non-black pixels in the active pixel's set. This parameter is more representative of the particle concentration as it takes into account the particle size. The projection is made in the same way it is performed in volume reconstruction. The particles are advected using a Runge–Kutta 45 algorithm. The velocity field used is an ABC flow defined by

$$u(\boldsymbol{X}, t) = A\sin(kZ) + C\cos(kY)$$

$$v(\boldsymbol{X}, t) = B\sin(kX) + A\cos(kY)$$

$$w(\boldsymbol{X}, t) = C\sin(kY) + B\cos(kX)$$

with $A = \sqrt{3}$, $B = \sqrt{2}$, $C = 1$ and $k = 1/20$. The images are 300×300 pixels and the volume is 238×238×72 voxels. The calibration model is a pinhole model, without distortions. Four cameras are used, set regularly on a circle and viewing the volume at a 30° angle with the Z axis.

3.2. Correlation algorithm

The correlation algorithm is iterative and multi-grid, with signal-to-noise ratio validation and median filter. The main goal was to compare the velocity field computed using the reconstructed volumes and the ones obtained with the original synthetic volumes. The time interval dt between the two exposures was found best equal to 1, leading to around 4 voxels for the maximum particle displacement. The interrogation window size is chosen equal to 24^3 voxels. These values are not universal, but they are the best in this case for the correlation algorithms and this velocity field. The particle size corresponds to 23 voxels particles, equivalent to a particle diameter of 3.5 voxels. For a seeding density of 0.001 ppv, the number of particles per interrogation window is equal to 12.

3.3. Quality evaluation

The quality of the reconstruction algorithm is evaluated through several quantities.

- *Reprojection quality* Q_i. It is computed as the normalized cross-correlation between the original images and the projections of the reconstructed volume. It characterizes the convergence of the algorithm, but not the accuracy of the solution.

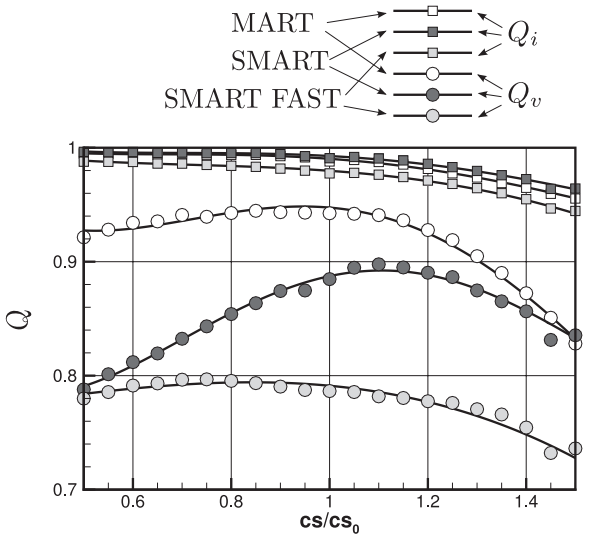

Figure 2. Evolution of the volume reconstruction quality with the voxel size divided by the reference voxel size (computed by the program).

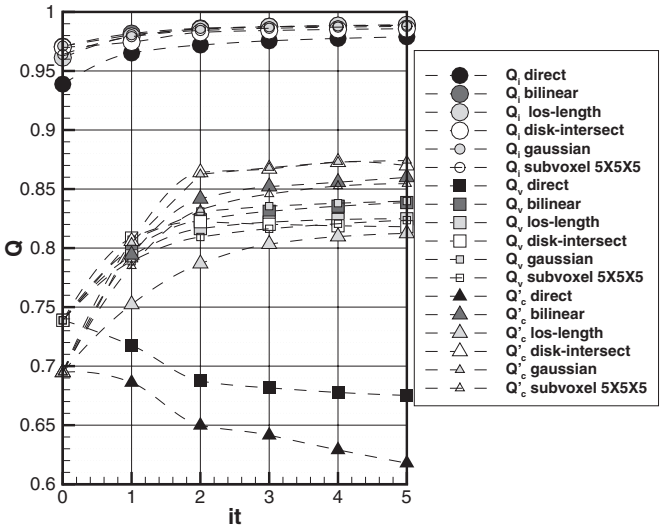

Figure 3. Evolution of the quality factors with the number of MART iterations for the different projection discretization methods.

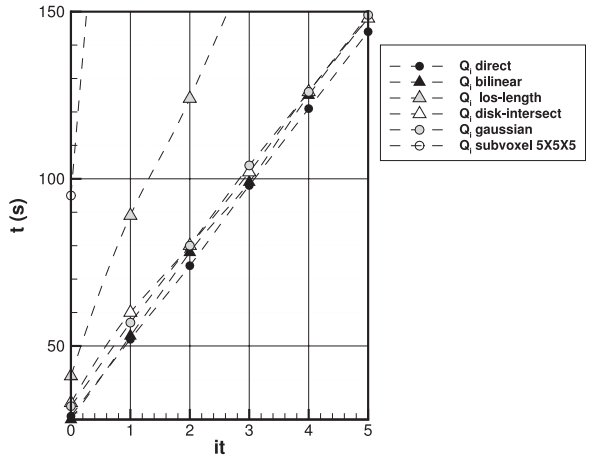

Figure 4. Reconstruction time for the different projection discretization methods.

- *Reconstruction quality* Q_v. It is computed as the normalized cross-correlation between the original volume and the reconstructed one. It is independent of the volume discretization as the reference volume is computed from the list of particle locations and discretized using the same grid as the reconstructed volume.
- *Correlation quality* Q'_c. The quality of the velocity field can be computed similarly to the previous quality factors (normalized cross-correlation Q_c). However, as the field is vectorial, a normalized cross-correlation compares only the angle and not the magnitude. For that reason, Q'_c is defined as the ratio between the root-mean-square difference between the velocity field computed using the synthetic volumes $\mathbf{u}_{\text{corr}}$ and the analytical one $\mathbf{u}_{\text{ref}}$ and the root-mean-square difference between the velocity field computed using the reconstructed volumes $\mathbf{u}_{\text{reconstruct}}$ and the analytical one:

$$Q'_c = \sqrt{\frac{\sum_i ||\mathbf{u}_{\text{corr}i} - \mathbf{u}_{\text{ref}i}||^2}{\sum_i ||\mathbf{u}_{\text{reconstruct}i} - \mathbf{u}_{\text{ref}i}||^2}}. \quad (14)$$

This quantity is used in order to eliminate the correlation algorithm errors and consider only the influence of the volume reconstruction quality on the velocity field computation.

3.4. Volume discretization

In this study, only cubic voxels were considered of size cs. The volume is discretized such that the voxel projection size is approximately equal to 1 pixel. In general, this cannot be true inside the whole volume, since the voxel projection size depends on the distance of the voxel from the camera. Therefore, in this analysis, the largest voxel projection size is equal to 1 pixel. This voxel size gives a projection to 1 pixel and is labeled as having size cs_0. The influence of the volume discretization is presented in figure 2. The effect of the voxel size on Q_i and Q_v is shown for the MART, SMART and SMART_FAST algorithms. Concerning Q_i, the smaller the voxels, the better the reprojection is. However there is only marginal improvement for $cs/cs_0 < 1$. The computation time is inversely proportional to the voxel size. When the reconstruction quality Q_v is considered, there is an optimal value; for MART, this is around 1, but if the voxels are smaller, the quality stays acceptable. For SMART_FAST, the optimum is around 0.8, but below 1 it is almost constant. For SMART, the optimum is around 1.1, with a rather pronounced peak. The value cs_0 generally chosen for the voxel size seems to be a good compromise between the computation time and reconstruction quality.

3.5. Projection discretization

The influence of the projection discretization is considered in terms of the quality (figure 3) and computation time (figure 4).

Concerning the reprojection quality Q_i, all the discretizations are equivalent except the direct method, which is to the point where we recommend it is unusable. The

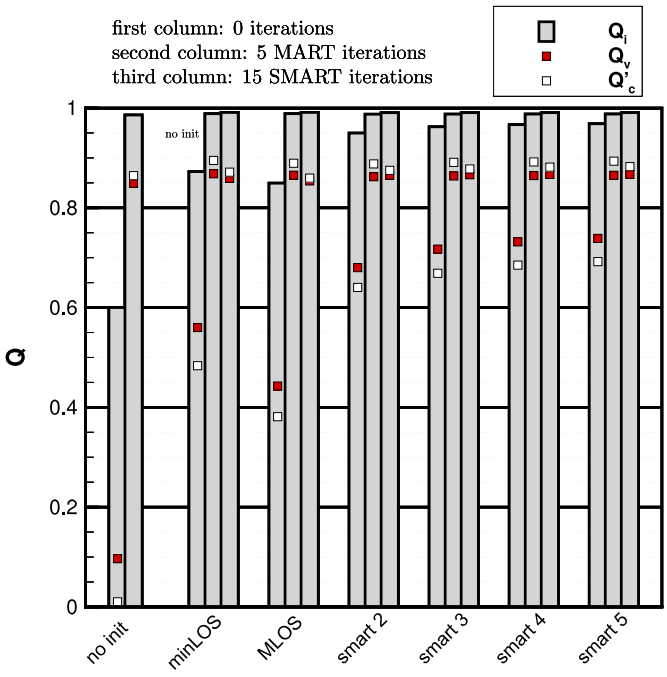

Figure 5. Influence of the initialization of the algorithms on the different qualities.

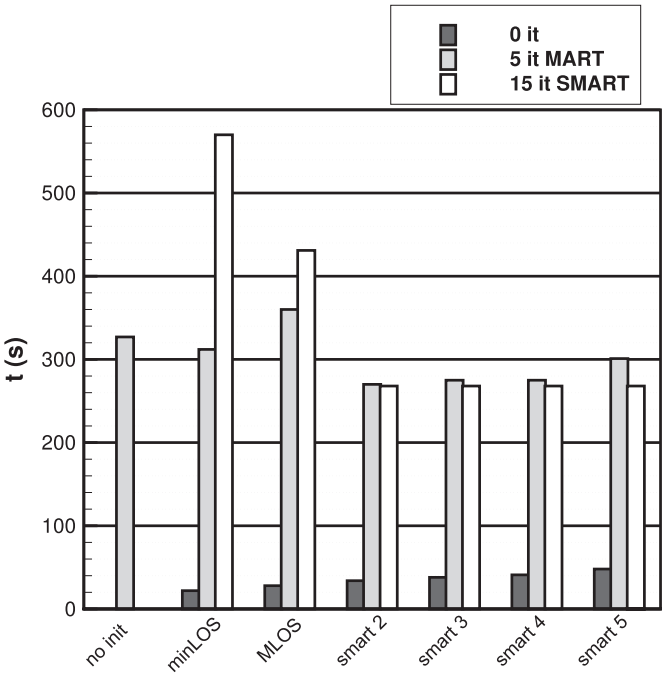

Figure 6. Influence of the initialization of the algorithms on the reconstruction time.

reconstruction quality is much more influenced by the projection discretization. The best results are obtained using the bilinear and the Gaussian weighting functions. Eventually, the correlation quality is the best for the disc-intersect and the Gaussian weighting functions. The los-length method is less precise than the others and should not be used.

Concerning the computation time, except for the los-length and the subvoxel methods, the computation time is more or less equivalent. The direct method is the fastest, but not by far.

3.6. Initialization

The initialization of the algorithm can have a great influence on the final solution of the problem, as there can be several, and on the computation time. This has been reported in figures 5 (for the quality) and 6 (for the computation time). SMART *n* represents an initialization modification that encompasses a minLOS first step and then *n* iterations of SMART_FAST.

Figure 5 compares the initial solution and also the solution after 5 MART iterations and 15 SMART iterations. SMART_FAST initialization gives the best initialization. However, at the end of the reconstruction algorithm, the differences are not so obvious in terms of quality. minLOS and SMART 5 lead to the same reconstruction quality, but the correlation quality is slightly better with SMART 5. MLOS gives a little lower quality, and the 'no init' result is below MLOS. The main differences are in terms of the computation time. SMART 4 is more efficient (around 15% faster), because it eliminates quickly some voxels with low intensity. With this initialization, 5 MART iterations is equivalent to 15 SMART iterations. With only minLOS, SMART is slower than MART.

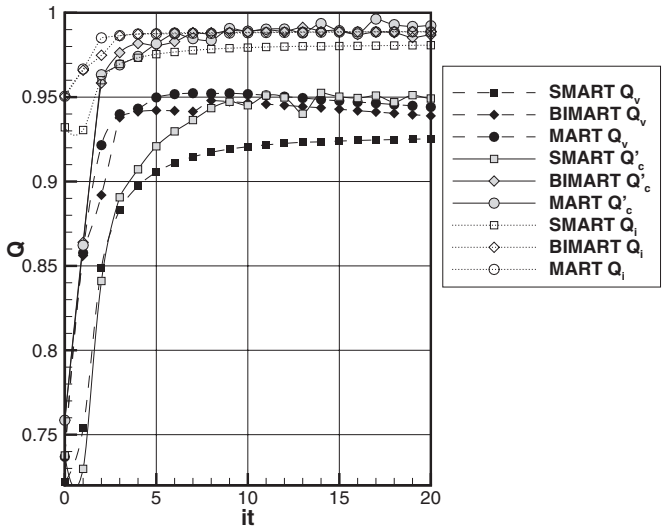

Figure 7. Evolution of the qualities with the number of iterations. Comparison of different algorithms.

3.7. Number of iterations

The number of iterations needed to converge is different for the algorithms. The convergence is shown in figure 7. The best reconstruction quality that can be obtained in these data is 92% for SMART, 94.5% for BIMART and 95.5% for MART. The number of iterations needed to reach this maximum is 8 for MART and BIMART and 20 for SMART. Five MART iterations are equivalent to eight BIMART iterations. The reprojection quality is around 98.5% for MART and BIMART and 98% for SMART, showing that the convergence is equivalent. The maximum correlation quality is 95% for SMART after nine iterations and 97.5% for BIMART after two iterations. The MART correlation quality is still increasing

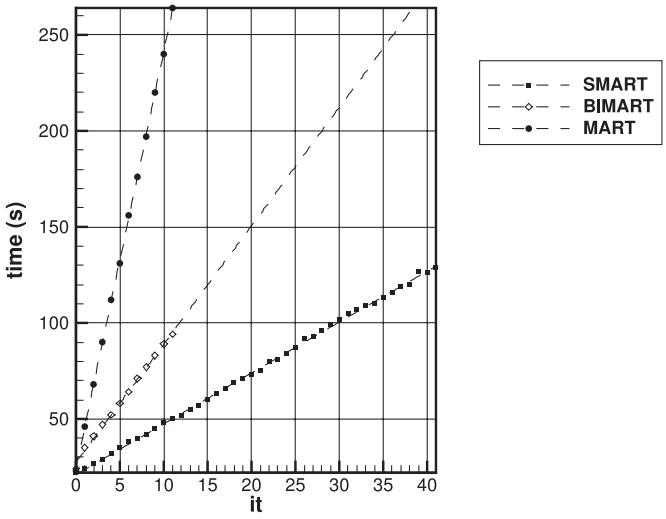

Figure 8. Evolution of the computation time with the number of iterations. Comparison of different algorithms.

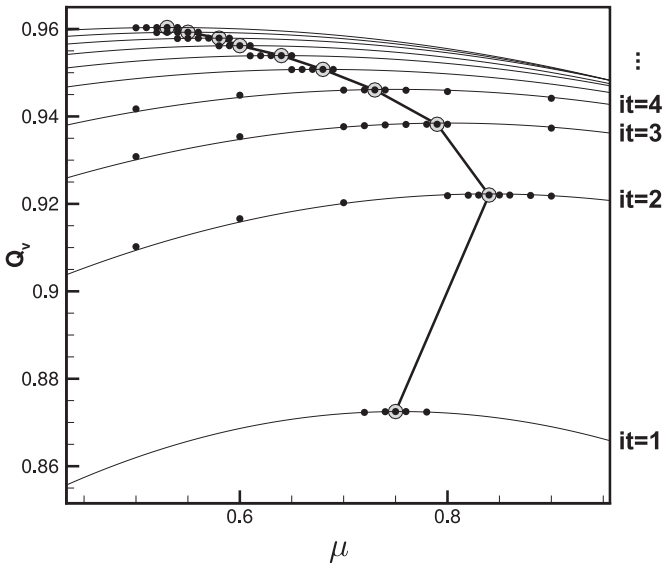

Figure 9. Optimization of the relaxation parameter. For each number of iterations (MART algorithm), the curves show the variation of Q_v with the relaxation parameter μ. The gray dots are put on the maximum values of Q_v for each total number of iterations (given on the right).

after 11 iterations where it reaches 98%. Hence MART in general converges toward a better solution, but it is closely followed by BIMART. SMART seems to be slightly less accurate.

As a standard test case, we use 5 iterations for MART, 8 iterations for BIMART and 15 iterations for SMART. Considering these values, the computation time is presented in figure 8. Five MART iterations take 132 s on a single 2.8 GHz CPU, while it takes 77 s (almost 50% gain) to compute eight BIMART iterations. This is equivalent to 20 SMART iterations. SMART is faster than the other algorithms, because all images simultaneously update the reconstruction field, but the accuracy is lower, due to the difficulty we have had to find an appropriate filtering of the volume. BIMART is a good compromise: its accuracy is equivalent to MART and the computation time is comparable to SMART.

3.8. Relaxation parameter

The relaxation parameter μ is usually taken equal to 1. Nevertheless, its optimal value depends on the number of iterations. This influence is evaluated in figure 9 with the reconstruction quality.

For each iteration number, the optimized value of μ is obtained. It can be observed that the optimal values vary with the number of iterations it. The optimal reconstruction quality at each step is always increasing, and after two iterations the optimal relaxation parameter decreases monotonically, otherwise, the algorithm does not converge any more. The same kind of evolution can be observed for the different reconstruction algorithms tested in this paper. The law for $it > 1$ is given in equation (15):

$$\mu = a\, it^{-b} + c. \tag{15}$$

The specific coefficients a, b and c are given in table 1.

The same study can be performed for SMART, but the law is much less regular and the relaxation parameter value is in general larger than 1. This value is less stable in the sense that if the relaxation parameter value is slightly increased, the algorithm can diverge severely. For 15 and more iterations, the coefficients are given in table 1.

Table 1. Coefficients of the law giving the relaxation parameter as a function of the number of iterations (equation (15)).

Algorithm	a	b	c
MART	0.986	0.150	0
BIMART	0.809	0.354	0
SMART	2.28	0.410	0
SMART_FAST	8.71	0.422	1.07

3.9. Volume filtering

Two filters are considered here. The first type, vt, is a threshold of the volume using a level vtl, considering that the intensities are normalized between 0 and 1. The second filter, called the volume Gaussian filter vgf, is a 3×3 Gaussian filter applied on each slice perpendicular to Z in the volume. It was introduced first by Discetti and Astarita (2011b) as the spatial filtering improved tomographic (SFIT)-PIV. The effect of the volume threshold is shown in figure 10, without Gaussian filtering (black symbols) and with Gaussian filtering (white symbols). The volume threshold filter, applied without Gaussian filtering, when the SMART 4 initialization is used, decreases all the qualities (reprojection, reconstruction and correlation) and does not speed up the reconstruction. When combined with the volume Gaussian filter vgf, the quality can be neatly increased in the MART case, but in the SMART case, it is more difficult to improve the result because of the slower convergence and the gain is lower. Concerning the threshold value, there is an optimum around 0.8% of the volume maximum intensity, but this value is not universal and depends on the seeding density.

The effect of the frequency of vgf against the number of iterations was investigated. The best strategy that we found to

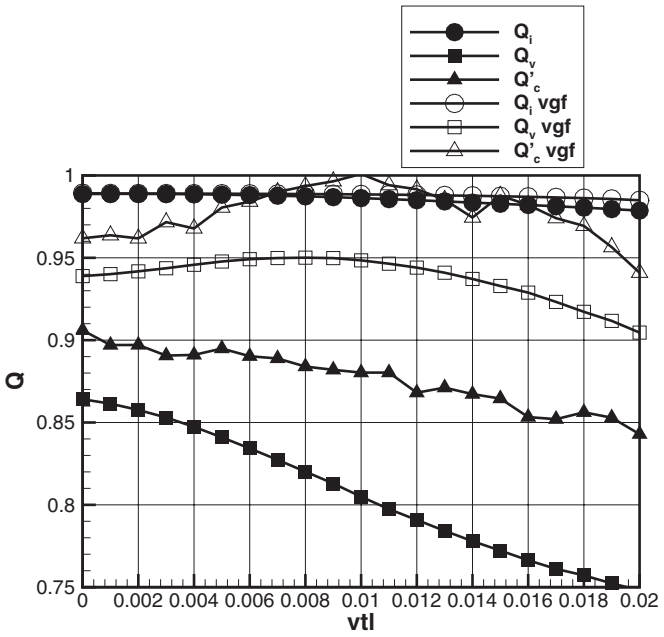

Figure 10. Influence of the volume threshold filter level on the reconstruction algorithm quality, with and without volume Gaussian filter.

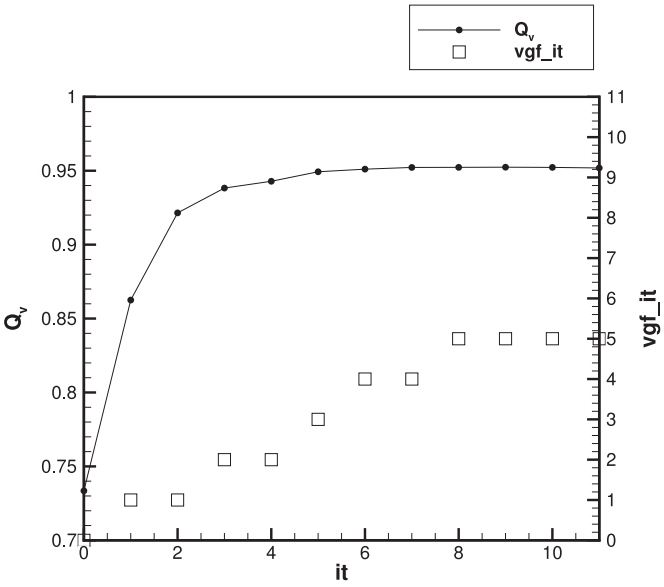

Figure 11. Best value (in terms of Q_v) of the number of iterations (vgf_it) during which is applied the volume Gaussian filtering, for each total number of MART iteration (it).

increase the reconstruction quality Q_v using MART is to apply the filter only at the beginning of the algorithm. The number of steps during which it is applied vgf_it can be optimized as in figure 11. The vgf filter is applied after the iterations 0 to vgf_it (included). What is for sure is that the filter should not be applied after the last iteration. For SMART, it is better to apply it three times regularly spaced during the iterations, with the last filtering pass just before the last iteration. The threshold level can be optimized for each ppv value, leading to the curves given in figure 12. The values leading to the best reconstruction quality are the same for MART and BIMART,

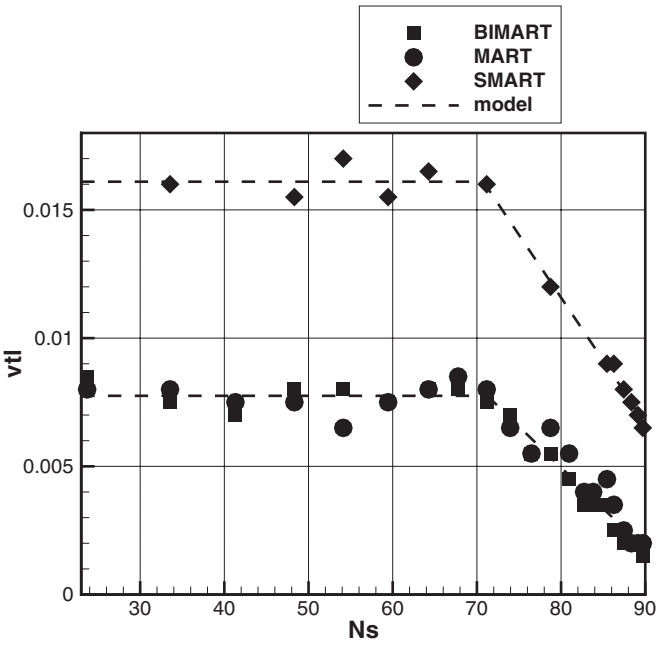

Figure 12. Optimized volume threshold level (vtl) as a function of the image signal ratio Ns.

Table 2. Coefficients of the law giving the volume threshold level as a function of the image signal ratio (equation 16).

Algorithm	a	b
(BI)MART	−0.031 9176	0.030 4891
SMART	−0.049 152	0.050 7119

but different for SMART. For signal image ratio (Ns) values lower than 70% (corresponding to a ppp equal to 0.05), the optimal value is constant (0.007 75 for MART and BIMART, 0.01 61 for SMART). For higher seeding density, the optimal threshold level decreases linearly. The expression is given in equation (16):

$$\text{vtl} = a\,N_s + b. \tag{16}$$

The specific coefficients a and b are given in table 2.

3.10. Extra volume thickness and noise

In the previously discussed sections, the laser sheet was modeled as a square/'top hat' function. When the images are perfect, it should be enough to restrict the reconstruction to the illuminated volume. In all experimental cases, there is inherent noise in the data, arising from diffusion, soft edges on the laser sheet, optical aberrations, defocused particles, to name a few. It is a good practice to ensure that the laser sheet profile intensity can be correctly reconstructed, and to show this one must reconstruct a region thicker than the prescribed laser sheet thickness. If the laser sheet is located between $Z_{\min}$ and $Z_{\max}$, while the volume is reconstructed between $Z_{\min} - \Delta Z$ and $Z_{\max} + \Delta Z$, the volume enlargement is defined as $\frac{\Delta Z}{Z_{\max} - Z_{\min}}$, where ΔZ is the added volume thickness. Only the part of the volume inside the laser sheet is compared to the synthetic volume. This is shown in figure 13. It represents the impact of the volume enlargement on the reconstruction quality for

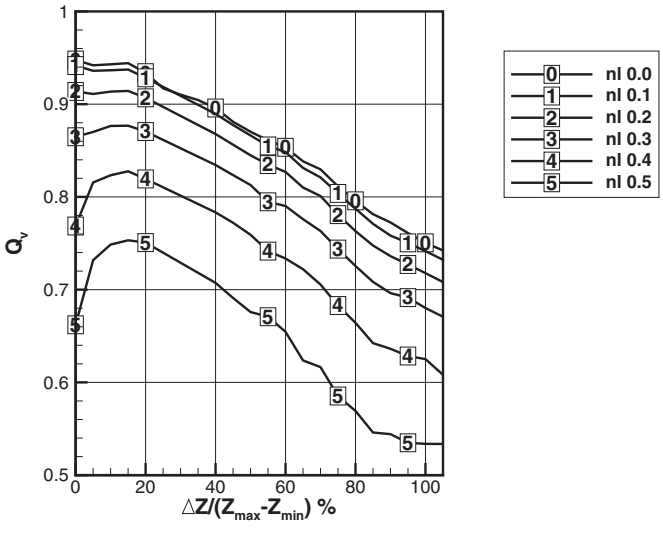

Figure 13. Evolution of the reconstruction quality with the volume enlargement for different noise levels.

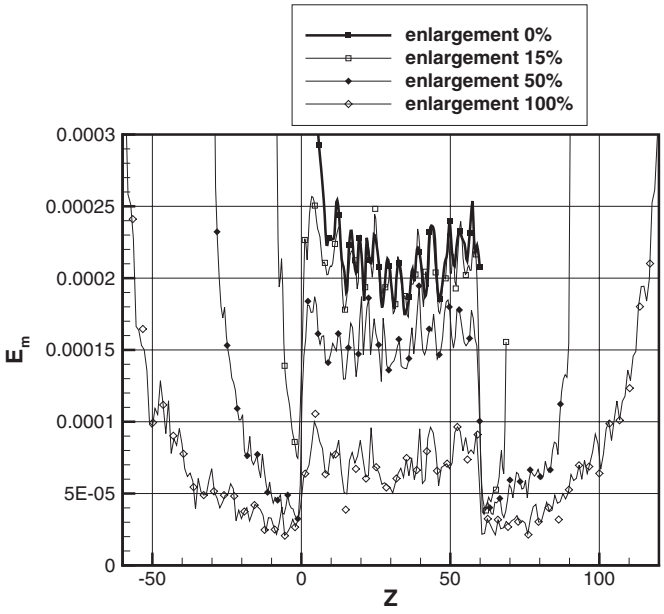

Figure 14. Reconstructed laser sheet intensity profiles for a 40% noise level for different volume enlargements.

different noise levels. When there is no noise, or 10% of noise ($nl = 0.1$), the reconstruction quality does not change much when a thicker volume is reconstructed. However, in the presence of a stronger noise, the reconstruction quality reaches a maximum for a volume enlargement of around 10%. The improvement gets better as the noise level increases. In experiments, noise is always present, hence the reconstruction should always be enlarged by 10% compared to the laser sheet thickness. It is possible to understand this result by looking at the laser sheet intensity profile. It is computed as the average intensity along the XY planes along Z, of the non-zero voxel values. The result for a 40% noise level is presented in figure 14 for several enlargements. Without any volume enlargement, the voxel energy is observed to increase near the

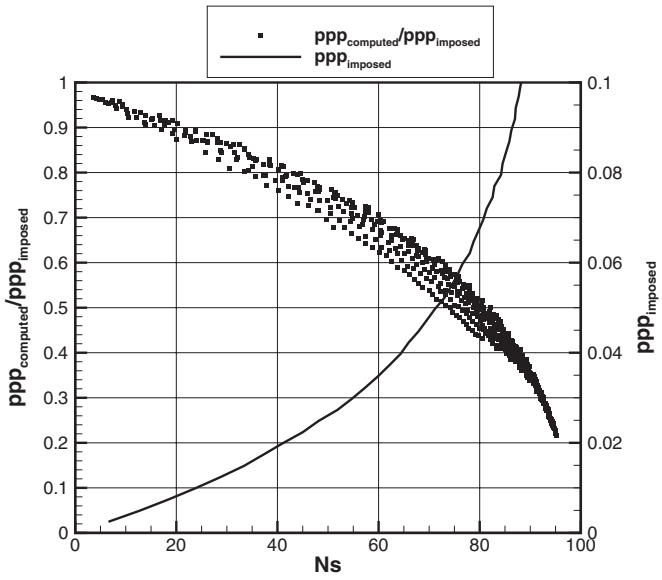

Figure 15. Saturation of the signal in the images when increasing the seeding density.

volume edges. With 15% enlargement, the profile is constant inside the original volume. When increased by more than the volume thickness, the profile stays flat, but the global level inside the volume divided by the minimum level outside the original volume, this quantity giving a signal-to-noise ratio, decreases. This can be explained as that the contrast between real and ghost particles decreases, leading to a poorer volume reconstruction.

3.11. Seeding density and particle size

The influence of the seeding density is important for two reasons. The first one is a practical one: it is impossible to estimate the particle concentration from the images for high densities because of their saturation as illustrated by figure 15. Figure 15 shows the ratio between the ppp obtained with the local peaks counting, and the exact ppp, as a function of the image signal ratio Ns. The number of particles detected tends to decrease with respect to the real number of particles as the image signal ratio increases. That means the experimental ppp is not really an adequate indicator of the number of particles per voxel (ppv). Ns is a better indicator to predict the reconstruction quality that can be obtained, because it takes into account the particle size. The evolution of the quality of the reconstruction is given in figure 16 for different algorithms. The reprojection quality is equivalent for all algorithms and it increases with Ns. The Q_v drops rapidly as Ns increases. It decreases faster for SMART than for MART. If one considers also the correlation quality, a limit of 90% gives the limit in terms of Ns slightly above 80% for MART and BIMART, and around 65% for SMART.

In figure 17, the reconstruction time for SMART and BIMART (for different block sizes) is compared. SMART and BIMART are faster than MART until Ns reaches around 85%. SMART is the fastest, and for $Ns = 70\%$, the computation time is 2.2 times higher than for MART. The choice of the block size

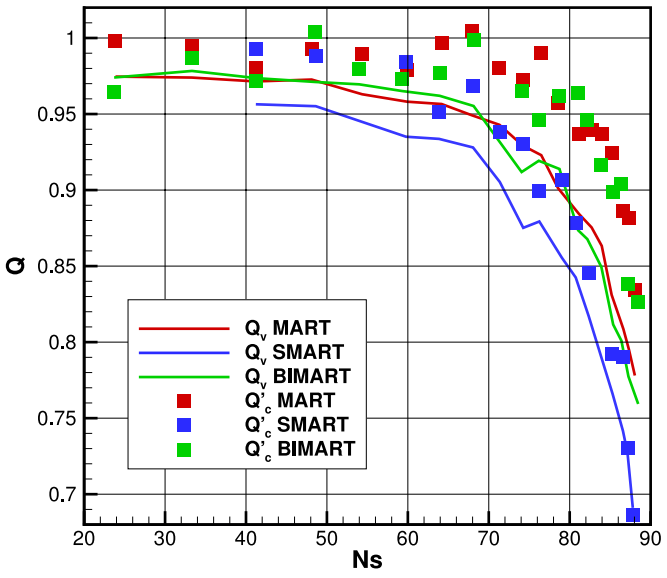

Figure 16. Evolution of quality with the image signal ratio *Ns* for the MART, SMART and BIMART algorithms.

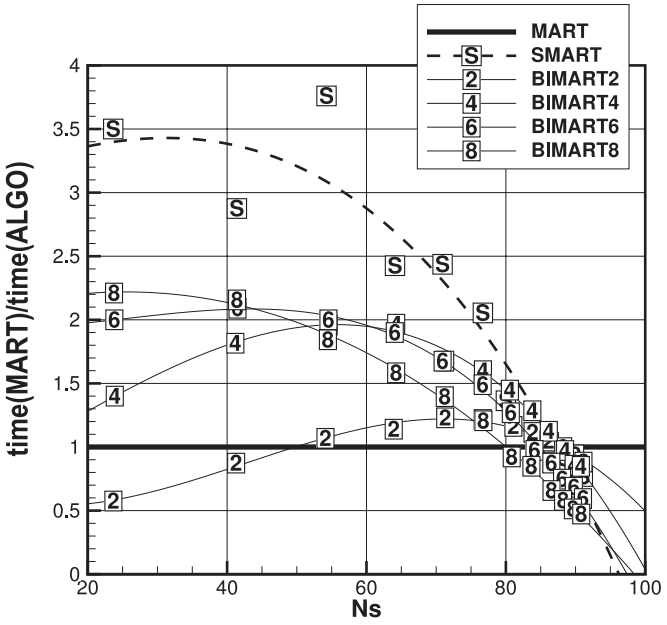

Figure 17. Relative evolution of computation time with the image signal ratio *Ns* for the MART, SMART and BIMART algorithms. The ordinate is the ratio between the computation time needed to reconstruct a volume with MART and the time needed by the other algorithm. For MART, this value is always equal to 1.

for BIMART depends on the seeding density. The lower the density, the bigger the blocks should be. However, for typical Tomo-PIV density, a block size of 4 seems to be the best choice as it corresponds to the particles' size in the images. The best strategy for choosing the blocks would consist in associating a block to each particle in the image. For $Ns = 70\%$, the computation time gain is 1.8, which is similar to SMART, for a better quality.

The particle size has also an influence on the image signal ratio. For a typical ppv value of 0.001, the influence of the particle size (via the number of voxels per particle (vpp)) on the

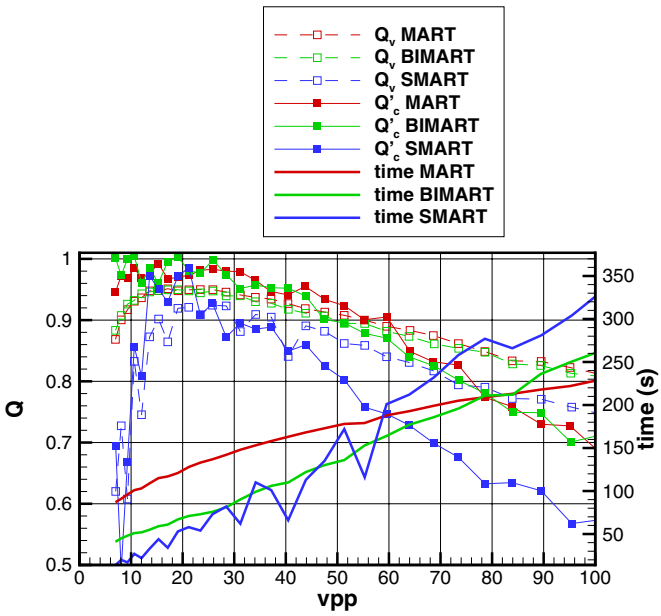

Figure 18. Evolution of quality and reconstruction time with the number of voxels per particle (vpp) for the MART (red), SMART (blue) and BIMART (green) algorithms.

qualities and the reconstruction time is investigated in figure 18. The reconstruction quality is a constant in the range of 15–25 vpp (diameter between 2.4 and 3.2 voxels). Over this range, the quality decreases linearly. Globally, the quality is higher for MART and BIMART and the results are slightly more stable than for SMART. The useful range is wider for MART and BIMART. The correlation quality has a similar behavior except for small particles. The quality is comparable to the best results for MART and BIMART. For SMART, the correlation robustness does not compensate the loss in the reconstruction quality. Concerning the reconstruction time, MART is slower than BIMART, which is comparable to SMART.

3.12. Cameras

The position of the cameras is a key parameter to consider as it cannot be modified *a posteriori*. It should be optimized during the experiment setting. The first parameter to be optimized is the cameras' spatial arrangement. Five configurations are shown in figure 19 and the results are presented in figure 20. In the first configuration (four cams, single plane (squares)), the cameras are in a single plane perpendicular to Y. They are on the same side of the volume and the angle between two adjacent cameras is constant. The optimum angle was found to be 22°.

In the second configuration (n cams, circle (circles)), the cameras are regularly placed along a circle, with the same viewing angle. With three cameras, the optimum is around 20°, while for more cameras (four, five and six), it is around 28°.

In the third configuration (four cams, one cam moving (triangle)), the second configuration with four cameras is considered. Two cameras are in the XZ plane and two are in the YZ plane. One camera in the X plane is moving in this plane.

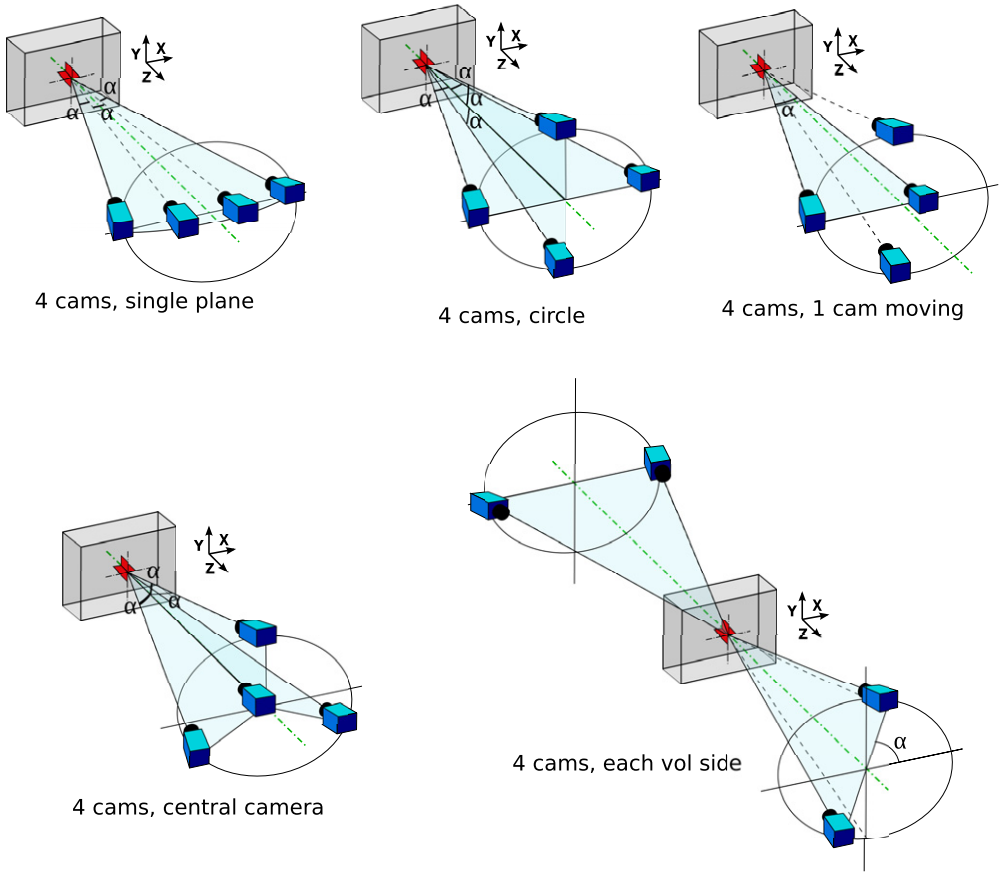

Figure 19. Sketch of the five different cameras' configurations studied.

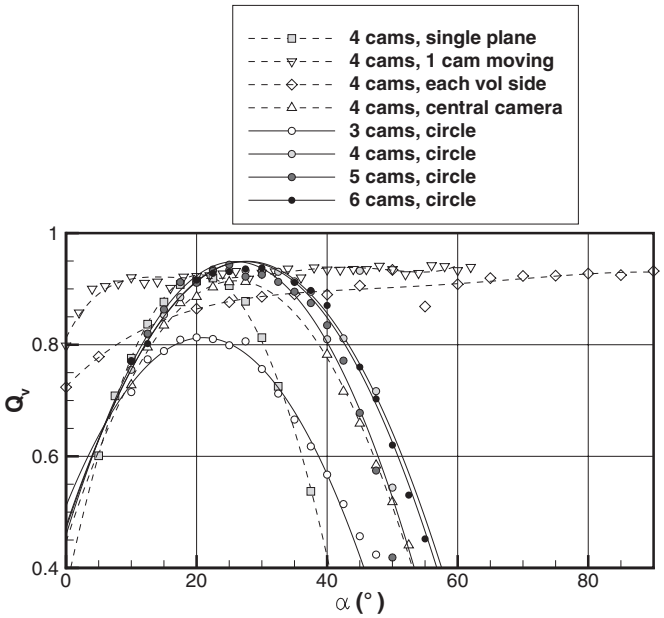

Figure 20. Comparison in terms of reconstruction quality of four cameras' configurations.

For an angle equal to 0, the camera is close to the same position as the other camera and for 60°, it corresponds to the (four cams, circle) configuration. The best position is the symmetric configuration (four cams, circle) (second configuration).

In the fourth configuration (four cams, central camera (pyramid)), a central camera is added compared to the second configuration. The viewing angle is varied. The best angle is also around 28°, but the reconstruction quality is lower. This configuration is more compact, but leads to lower quality.

In the fifth configuration (four cams, each vol side (diamonds)), two cameras are on one side, in the XZ plane, with a 30° viewing angle. Two other cameras are on the other side of the volume in the same plane. The angle varying is between the cameras' planes. When equal to 0°, the four cameras are in the same plane; for 90°, the two cameras planes are perpendicular. The best angle is when the planes are perpendicular, giving a result equivalent to the configurations where the cameras are on the same side. The best configuration is the configuration 2, with a 28° viewing angle for each camera. The effect of Mie light scattering (that modifies the particles' intensity on the images) on the cameras' best position can be found in de Silva *et al* (2012).

Another numerical experiment concerns the number of cameras and the evolution of reconstruction quality with the volume thickness (with the same ppv). The results are given in figure 21, as a function of the laser sheet thickness. Clearly, the quality loss due to the increases of volume thickness is lower when there are more cameras. Eventually, the influence of one camera calibration error (angle deviation) is shown in figure 22. An error in one camera angular position has dramatic effects on the reconstruction quality. The maximum error that can be allowed is no more than 0.5° (corresponding

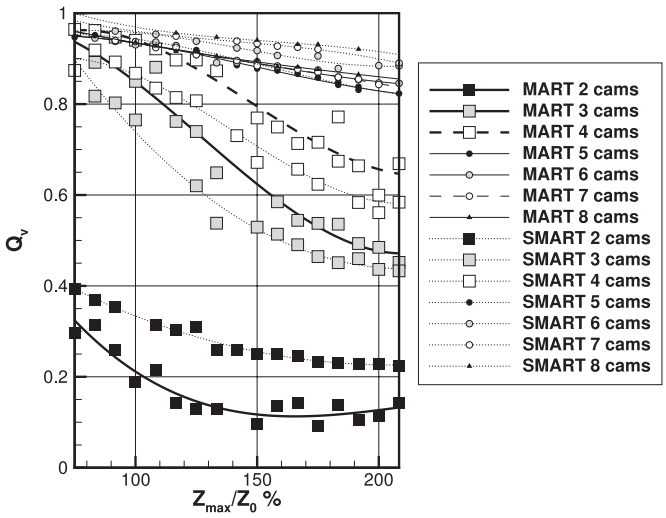

Figure 21. Comparison in terms of reconstruction quality for different camera numbers and volume thicknesses.

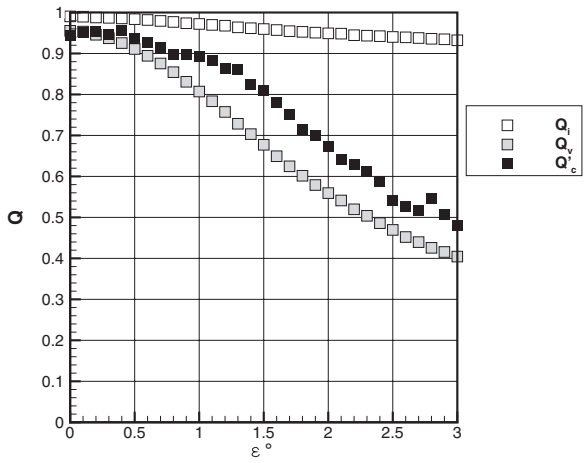

Figure 22. Influence of a calibration error of one camera on the reconstruction quality.

to a maximum localization error of one particle radius in one image (on the edge)). It is interesting to observe that the angular error modifies largely the reconstructed laser sheet profile, as shown in figure 23. The ratio between the intensity in the laser sheet and outside decreases, proving an intensification of the ghost particles' intensity.

Different parameters influence the particle volume reconstruction and modify the quality of the reconstruction. Similar to the results for numerical data, it is also important to validate these on real data.

4. Experimental results

The findings from section 3 are applied to some experimental measurements. A pulsed jet in cross flow was used to compare different techniques. The experimental setup is described in Vernet *et al* (2009). The jet in a cross-flow experiment takes place in a water channel. A horizontal flat floor was placed in the channel to generate a 20 mm thick boundary layer close to the jet nozzle. The square jet of $L = 30$ mm width has a mean

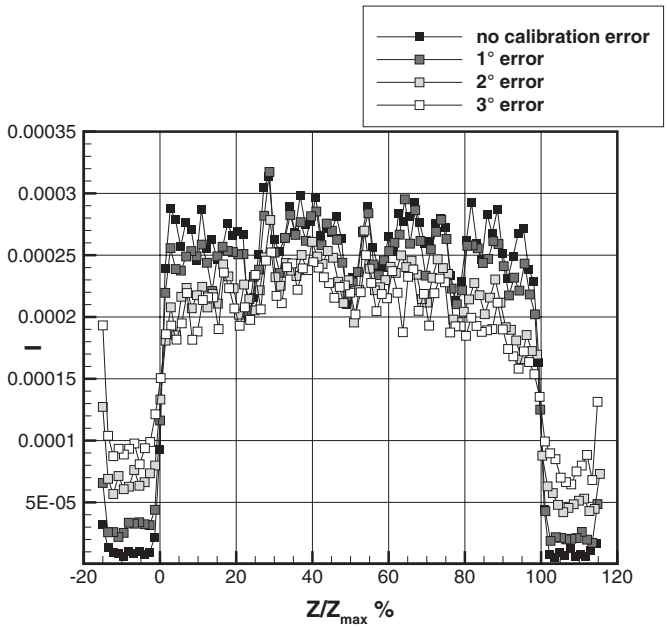

Figure 23. Influence of a calibration error of one camera on laser sheet profiles.

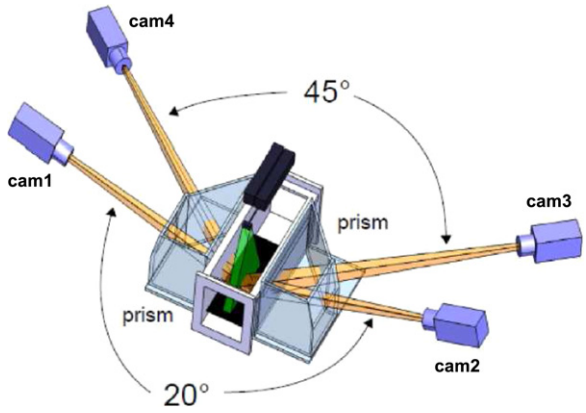

Figure 24. Cameras' setup used for Tomo-PIV measurements.

injection velocity $\overline{U}_j$. It is pulsed at 1 Hz frequency, with an amplitude giving a jet velocity varying between 0 and $2\overline{U}_j$. The non-dimensional numbers (equation (17)) characterizing the flow are the jet-to-cross-flow ratio R between the mean jet velocity $\overline{U}_j$ and the cross-flow velocity U_{cf} ($R = 1$) and the Reynolds number Re_j based on the mean jet velocity, the characteristic length L (defined as the length of the square orifice) and the kinematic viscosity ν ($Re_j = 500$):

$$Re_j = \frac{\overline{U}_j L}{\nu} \qquad R = \frac{\overline{U}_j}{U_{\mathrm{cf}}}. \tag{17}$$

The measurement setup consists of four 1600×1200 cameras, coupled with a 200 mJ Nd:YAG laser. The 25 mm laser sheet is coming from the top; the cameras' configuration is shown in figure 24. Some prisms are added on the channel walls to prevent image astigmatism.

Several preprocessing techniques were tried, but only two were presented here. Two sets of images were used:

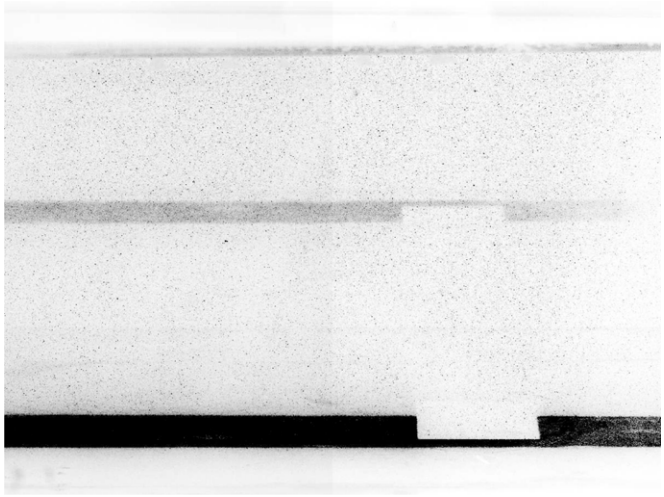

Figure 25. Example of raw acquisition image.

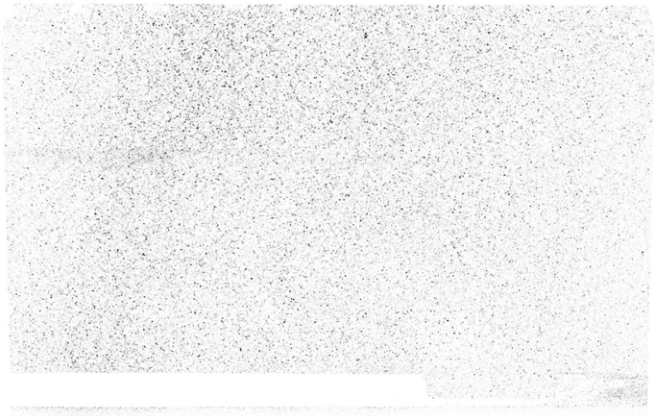

Figure 26. Example of image filtered with a background subtraction (computed using a temporal median filter of size 5 on five images).

- raw images (leading to large reconstruction times) and
- filtered images, reducing the strong reflections in the images for the two cameras 1 and 2 (see figure 24) and using a temporal median filter with five images on each pixel to compute the background.

The effect of the preprocessing is shown in figures 25 and 26. The gray levels are inverted. The background subtraction eliminates the reflections, but creates at the bottom of the images a black region corresponding to the laser reflection at the bottom of the tank, hence a black region is introduced in the volume. A misalignment correction was applied, decreasing the calibration misalignment errors from around 3 pixels to less than 0.1 pixels. The BIMART algorithm (block size 4) with eight iterations is used. The relaxation parameter is set automatically to 0.388. A volume Gaussian filtering is applied and the threshold filter is automatically set to 0.004. The resulting volume size is $1041\times645\times202$ voxels with 2.74×10^{-3} mm^3 voxel volume. The images are characterized by ppp $\simeq$ 0.048 and $Ns \simeq 83\%$. The rather high density and reflections make it difficult to obtain good results. The correlation final interrogation window size is $48\times48\times48$ with 75% overlap. Two results are presented: one without

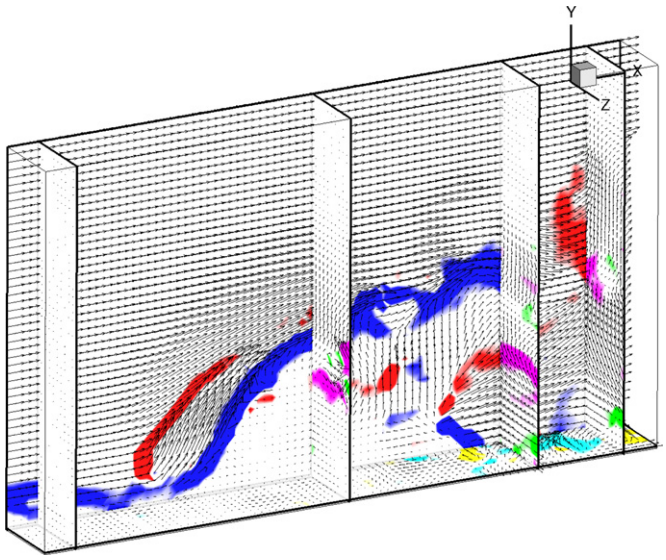

Figure 27. Example of velocity field, computed without misalignment correction, with vorticity component perpendicular to the plane image iso-contours.

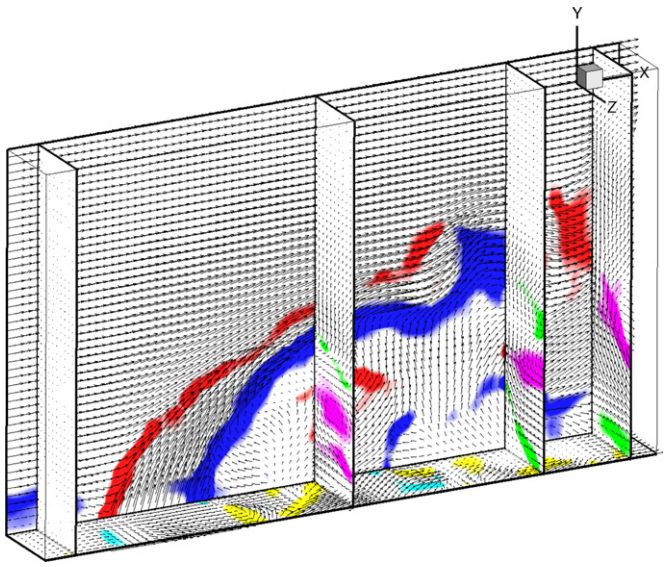

Figure 28. Example of velocity field, with vorticity component perpendicular to the plane image iso-contours.

the misalignment correction (figure 27) and one with (figure 28). The iso-contours of vorticity component perpendicular to the plane considered are displayed with different colors. The visible areas correspond to a vorticity level above 1 s^{-1}. The enhancement of the result is obvious from a physical point of view: even if the symmetry plane is rather similar, the longitudinal structures do not exist in the uncorrected fields, while they appear clearly in the corrected one. The final velocity field shows the typical structures usually present in the jet in cross flow. The entrainment under the jet is clearly visible.

5. Discussion

In the literature, several parametric studies have already been performed. Elsinga and others performed 2D simulations, and for example Worth and Nickels (2008) showed that the results for Q_v are lower in 3D. The results depend also on the particle size. Hence, it is not always easy to compare the results.

The influence of several parameters has already been tested. The initialization was investigated by Worth and Nickels (2008), but the test was less extended. The use of the different weighting functions has not really been compared in the literature. The number of iterations, the seeding density, the image noise, the relaxation parameter, the 3D filtering and the camera angles were the principal parameters investigated. Globally, the present results are similar to the previous results, when it is possible to compare. The principal gains that are obtained here are as follows:

- there is a gain in stability of the reconstruction quality results till the limit of 0.05 ppp (*Ns* around 70%), which is the same as previous studies;
- BIMART, a generalized version of the classical algorithms, which is a good compromise between speed gain and accuracy;
- a new way to apply SFIT (Discetti and Astarita 2011b), not after each iteration but only at the beginning, and combined with a volume threshold;
- the relaxation parameter has to be adapted to the final number of iterations and
- the volume enlargement that reduces the impact of noise, which was something known in the community, but not studied and published systematically.

Some optimization results may not be universal, such as the vtl, the initialization with SMART_FAST or the SMART relaxation optimization, but at least, the experimentalists and the programmers are aware that some parameters can be changed in order to improve the reconstruction quality.

6. Conclusion

The MART algorithm family was studied and optimized. The generalization to BIMART is interesting, as the reconstruction time is comparable to the SMART reconstruction time, but with a better accuracy. The most favorable algorithm using the synthetic data presented herein was BIMART with block size equal to four, using eight iterations and with a disc-intersect or the Gaussian functions as the weighting functions. An initialization with minLOS is necessary to reduce the computation time. By adding a few iterations of a fast version of SMART (four typically), the computation time can be decreased slightly. It was found that the relaxation parameter should be carefully selected based on the number of iterations to ensure the most rapid convergence and to avoid divergence. During the reconstruction, a filter (during the five first iterations) combined with a threshold (given by equation (16) as a function of *Ns*) should be applied to improve the reconstruction and correlation qualities. A particle size of around 3 voxels in diameter is ideal to improve the correlation quality. The image signal ratio should not exceed 70% for 1% error on the velocity field and 80% for 5% error. Camera configurations should be carefully planned before undertaking experiments, with a viewing angle of $27^\circ \pm 7^\circ$ for four cameras in cross configuration and an angle of $21^\circ \pm 3^\circ$ for the planar configuration. The volume should also be reconstructed wider by 10% on each side than the laser sheet, especially for noisy data. A misalignment correction procedure must be applied systematically.

The BIMART algorithm can be parallelized easily because of its block architecture. This algorithm includes some *a priori* knowledge about the data to reconstruct (maximum of entropy, particles elongated in Z direction) but it would also be beneficial to add some stronger *a priori*, specifying that we want to reconstruct spherical particles. This has been partly proposed by Wieneke (2011). Another approach is MENT (Bilsky *et al* 2012), which would reduce drastically the memory consumption (and also the computation time), but still the reconstruction quality is lower than SMART. Also great care should be taken to apply the preprocessing of the images as the result (in terms of quality and computation time) depends strongly on our capacity to eliminate the background and keep only the particles. Recently, a new filtering procedure has been proposed by de Silva *et al* (2013) to eliminate *a posteriori* reconstructed particles: it should be tested if this filter is equivalent somehow to the combination of volume Gaussian filter and threshold proposed in this study.

Acknowledgments

This work was initially supported by the ANR Project VIVE3D and now by the EU-project: Advanced Flow Diagnostics for Aeronautical Research, project no 265695.

References

Atkinson C and Soria J 2007 *Proc. 16th Australasian Fluid Mechanics Conf. (Gold Coast, Australia)* pp 191–8
Atkinson C and Soria J 2009 *Exp. Fluids* **47** 553
Bilsky A, DM M, Tokarev M and Lozhkin V 2012 *16th Int. Symp. on Applications of Laser Techniques to Fluid Mechanics (Lisbon, Portugal)*
Byrne C 2009 *Int. Trans. Oper. Res.* **16** 427–63
de Silva C, Baidya R, Khashehchi M and Marusic I 2012 *Exp. Fluids* **52** 425–40
de Silva C, Baidya R and Marusic I 2013 *Meas. Sci. Technol.* **24** 024010
Discetti S and Astarita T 2011a *Exp. Fluids* **52** 765
Discetti S and Astarita T 2011b *9th Int. Symp. PIV (Kobe, Japan)*
Elsinga G 2008 Tomographic particle image velocimetry and its application to turbulent boundary layers *PhD Thesis* Delft University of Technology, The Netherlands
Elsinga G, Wieneke B, Scarano F and van Oudheusden B 2006 *Exp. Fluids* **41** 933
Gordon R, Bender R and Herman G 1970 *J. Theor. Biol.* **29** 471
Herman G 1980 *Image Reconstruction from Projections: the Fundamentals of Computerized Tomography* (New York: Academic)
Lamarche F and Leroy C 1990 *Comput. Phys. Commun.* **59** 359

Petra S, Schnörr C, Schröder A and Wieneke B 2007 *Proc. 6th Workshop on Modelling of Environmental and Life Sciences Problems (WMM 07, Constanta, Romania)* (Bucharest: Acad Romane)
Petra S, Schröder A and Schnörr C 2009 *Imaging Meas. Methods Flow Anal.* **106** 63
Scarano F 2013 *Meas. Sci. Technol.* **24** 012001
Schanz D, Gesemann S, Schröder A, Wieneke B and Michaelis D 2010 *15th Int. Symp. on Applications of Laser Techniques to Fluid Mechanics (Lisbon, Portugal)*
Thomas L, Vernet R, Tremblais B and David L 2010 *15th Int. Symp. on Applications of Laser Techniques to Fluid Mechanics (Lisbon, Portugal)*
Tremblais B, David L, Arrivault D, Dombre J, Chatellier L and Thomas L 2010 Slip: simple library for image processing (version 1.0) www.sic.sp2mi.univ-poitiers.fr/slip/
Verhoeven D 1993 *Appl. Opt.* **32** 3736–54
Vernet R, Thomas L and David L 2009 *Exp. Fluids* **47** 707–20
Wieneke B 2011 *9th Int. Symp. PIV (Kobe, Japan)*
Worth N and Nickels T 2008 *Exp. Fluids* **45** 847